10.1016/j.measurement.2020.107934

Measurement of indoor air temperature distribution using acoustic travel-time tomography: Optimization of transducers location and sound-ray coverage of the room

Najmeh Sadat Dokhanchi[a], Joerg Arnold [a], Albert Vogel [a], Conrad Voelker [a]

[a] *Department of Building Physics, Bauhaus-Universität Weimar, Coudraystraße 11a, 99423 Weimar, Germany*

Full Paper

The full article appeared in the journal *Measurement 164 (2020) 107934* and can be also found at https://doi.org/10.1016/j.measurement.2020.107934.

Abstract

Acoustic travel-time TOMography (ATOM) allows the measurement and reconstruction of air temperature distributions. Due to limiting factors, such as the challenge of travel-time estimation of the early reflections in the room impulse response, which heavily depends on the position of transducers inside the measurement area, ATOM is applied mainly outdoors. To apply ATOM in buildings, this paper presents a numerical solution to optimize the positions of transducers. This optimization avoids reflection overlaps, leading to distinguishable travel-times in the impulse response reflectogram. To increase the accuracy of the measured temperature within tomographic voxels, an additional function is employed to the proposed numerical method to minimize the number of sound-path-free voxels, ensuring the best sound-ray coverage of the room. Subsequently, an experimental set-up has been performed to verify the proposed numerical method. The results indicate the positive impact of the optimal positions of transducers on the distribution of ATOM-temperatures.

Measurement of indoor air temperature distribution using acoustic travel-time tomography: optimization of transducers location and sound-ray coverage of the room

Najmeh Sadat Dokhanchi[a,*,1], Joerg Arnold[a], Albert Vogel[a] and Conrad Voelker[a]

[a]Bauhaus-University Weimar, Department of Building Physics, Weimar, Coudraystrasse 11A, 99423, Germany

ARTICLE INFO

Keywords:
Travel-time tomography
Temperature distribution measurement
Image source model
Cross-correlating technique
Peak detection method
SIRT algorithm

ABSTRACT

Acoustic travel-time TOMography (ATOM) allows the measurement and reconstruction of air temperature distributions. Due to limiting factors, such as the challenge of travel-time estimation of the early reflections in the room impulse response, which heavily depends on the position of transducers inside the measurement area, ATOM is applied mainly outdoors. To apply ATOM in buildings, this paper presents a numerical solution to optimize the positions of transducers. This optimization avoids reflection overlaps, leading to distinguishable travel-times in the impulse response reflectogram. To increase the accuracy of the measured temperature within tomographic voxels, an additional function is employed to the proposed numerical method to minimize the number of sound-path-free voxels, ensuring the best sound-ray coverage of the room. Subsequently, an experimental set-up has been performed to verify the proposed numerical method. The results indicate the positive impact of the optimal positions of transducers on the distribution of ATOM-temperatures.

1. Introduction

To reconstruct the air temperature and flow velocity distributions of a fluid in a volume (three-dimensional problem), the technique of Acoustic travel-time TOMography (ATOM) can be applied [1, 2, 3, 4, 5]. ATOM utilizes the dependency of the speed of sound on air temperature and flow velocity in the medium. The average speed of sound, along the propagation paths, can be determined by travel-times estimation of a defined acoustic signal between transducers [6, 7, 8]. For discretization of the temperature and flow field, the tomographic domain is divided into volumetric grid cells called voxels. Subsequently, the spatial distribution of temperature and flow velocity within each voxel can be determined by applying a proper tomographic reconstruction algorithm [9, 10, 11, 12, 13].

The reconstruction of the air temperature distribution is a scalar tomographic problem, meaning that the scalar temperature influences the sound velocity independently of the direction of sound propagation [14, 15, 16, 17]. Unlike air temperature, calculation of the air flow must be described as a vector field tomographic problem. For this purpose, a separation of the scalar temperature from the air flow calculation can be derived by the method of reciprocal sound paths. In this method, a pair of transmitters and receivers provides the forward and backward propagation of sound waves. As a result, the flow velocity along the propagation paths is obtained by calculating the travel-time differences between reciprocal sound paths, leading to a simultaneous calculation of the air temperature and flow velocity [18, 12].

Application of the ATOM technique is employed primarily in outdoor environments by atmospheric sciences for the remote monitoring of meteorological quantities [19, 20, 21, 22, 23] while there is a great potential to use this technique for indoor climates. However, a small number of experiments on the ATOM have been performed to observe indoor air temperature distributions. Among them, [12] proposed a small scale two-dimensional tomographic system (four output channels and four input channels) for exploring the experimental arrangement of transmitters and receivers under laboratory conditions. Subsequently, this model is extended to a larger scale used in a building. Following of this approach, [4] resolved three-dimensional distributions of air temperature and flow fields within a certain volume. In this experiment, the same method of bidirectional sound-ray paths to calculate the influence of air temperature and flow properties was applied. More recent investigation was performed by [3] to determine spatially differentiated room air temperature with only one loudspeaker and one microphone with the intention to use as little hardware as possible. Although [3] utilized the visualization of the image source model (ISM) to find the proper location of transducers in terms of having homogeneous and distinguishable sound-ray paths, investigation of numerical estimation of optimal positions of the source and receiver is still required.

One primary factor, which has a major impact on the accuracy of the reconstructed temperatures, is the detection of the correct peaks in the room impulse response (RIR) reflectogram. This peak detection poses a challenge when the sound rays have similar travel-times. Therefore, it is required to control the distribution of the travel-times in the RIR reflectogram with the intention of travel-time separation.

This paper presents a novel numerical method to minimize the number of simultaneous arrival times of early reflections in the reflectogram by finding optimal positions of transducers, as their coordinates within the room geometry examined have a direct impact on the distribution of travel-times. For instance, in case of symmetry at the coordinates of transduc-

*Corresponding author
ORCID(s): 0000-0002-2657-4948 (N.S. Dokhanchi)
[1]email address: najmeh.sadat.dokhanchi@uni-weimar.de

ers, several sound paths may arrive simultaneously as they travel the same distance to reach the receiver. However, the proposed optimal positions have the minimum number of simultaneous arrival times within a threshold level, where the threshold level results from differences between the lengths of the sound paths. Furthermore, to ensure the best sound-ray coverage of the room, an additional function is employed to the proposed numerical method, which minimizes the number of sound-path-free tomographic voxels for the early reflections.

The organization of the paper is as follows. In section 2, the theoretical background of our approach is reviewed. Section 3 describes the presented numerical method. In section 4, the experimental set-up and measurement processing are outlined. Section 5 discusses the measurement results and data analysis. Finally, section 6 presents the conclusions.

2. Theoretical background

In this section, the method of the ATOM technique presented includes primarily the procedure of travel-times measurement and tomography reconstruction. First, travel-times between transmitter and receiver are estimated along the propagation paths, namely a forward problem. Second, the spatially distributed temperatures are reconstructed as an inverse problem using a proper tomographic algorithm. These forward and inverse problems of the ATOM technique [19] are detailed in the following.

2.1. Temperature dependent travel-time

The propagation of the sound wave in gas is mainly affected by the temperature and flow velocity [24]. Under adiabatic conditions, the speed of sound is given by

$$c = \sqrt{\gamma \cdot R_s \cdot T(1 + 0.513q)}, \tag{1}$$

where c is the Laplace speed of sound for dry air, $\gamma = 1.40$ is the ratio of the specific heat at constant pressure and volume of the gas, $R_s = 287.058\ Jkg^{-1}K^{-1}$ is the specific gas constant, q is the specific humidity which is the ratio of water vapor mass to the total mass of moist air, and T is the temperature of the gas in K [3, 25, 26]. Accordingly, (1) is used to determine the average air temperature along the propagation paths. To solve the forward problem of the ATOM technique, it is necessary to define the relationship between the speed of sound and the measured travel-times. Hence, the speed of sound can be derived experimentally from the travel-times estimation. ATOM employs the principles of geometrical acoustics to define the relationship between travel-times and the speed of sound [27]. The travel-time along the sound propagation paths can be expressed as the following integral form:

$$\tau = \int_l \frac{1}{c(r)} dl = \int_l s(r) dl, \tag{2}$$

where $c(r)$ is the spatially variable speed of sound, $s(r)$ is the slowness which is a reciprocal value of the speed of sound, l is the sound paths length, and r describes the position inside the tomographic area as a vector of x, y and z coordinates [11, 3, 4].

To extract the travel-time between the emitted and the received signal, the cross-correlating technique is used. The locations of the maxima in the cross-correlation function indicate the temporal lag between the transmitted and received signals, representing the travel-time of the signal [12, 28]. To improve the cross-correlation results, a maximum length sequence (MLS) is used as an excitation signal with the sequence length of 2n-1, where n is the number of digital shift registers. The MLS is a type of sequences that benefits from a perfect pulse auto-correlation characteristics, making it suitable for arrival time estimation [29, 30, 31]. The cross-correlation between $x(n)$ and $y(n)$ can be expressed as [24]

$$r_{xy}(m) = \frac{1}{N} \sum_{n=0}^{N-1} y(n)x(n-m), \quad m = 0, ..., 2N-2 \tag{3}$$

where $x(n)$ and $y(n)$ present the acoustic signal in discrete form at transmitting and receiving points respectively, each contained N samples and m is the lag index. The relation between the $x(n)$ and $y(n)$ can be formulated using convolution theory as [32]

$$y(n) = h(n) * x(n) = \sum_{k=0}^{\infty} h(k)x(n-k), \tag{4}$$

where h(n) is the impulse response of the system and k is a dummy variable of the summation argument representing the lags applied to $x(n)$. Therefore, based on 3 and 4, the cross-correlation function can be given by

$$\begin{aligned} r_{xy}(m) &= \frac{1}{N} \sum_n \left(\sum_k h(k)x(n-k) \right) x(n-m), \\ &= \frac{1}{N} \sum_k h(k) \left(\sum_n x(n-k)x(n-m) \right), \end{aligned} \tag{5}$$

The MLS signal has the following property [33, 34]

$$\begin{cases} \sum_n x(n-k)x(n-m) = N & \text{if } k = m; \\ \sum_n x(n-k)x(n-m) \simeq 0 & \text{if } k \neq m. \end{cases} \tag{6}$$

By applying conditions 6 in 5 it yields

If $k = m$, then

$$r_{xy}(m) = \frac{1}{N} h(k)N = h(m) \tag{7}$$

If $k \neq m$, then

$$r_{xy}(m) = \frac{1}{N} \sum_k h(k) \sum_n x(n-k)x(n-m) \simeq 0 \tag{8}$$

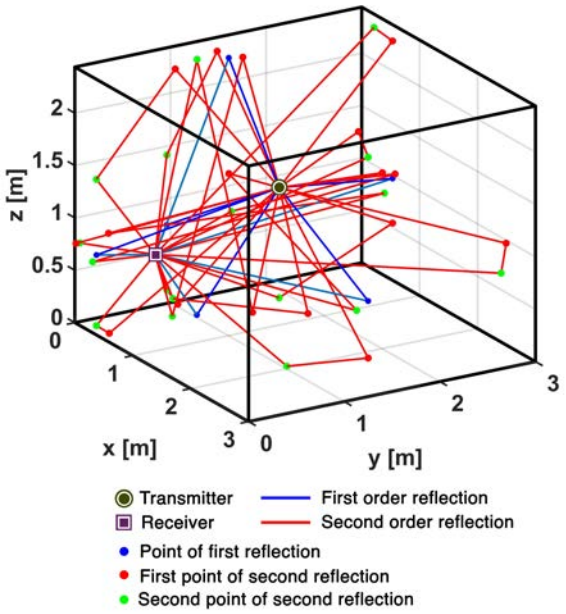

Figure 1: Three-dimensional representation of an image source model (ISM) with first and second order reflections.

2.2. Image source model (ISM)

Parallel to measurements, simulated travel-times are obtained by applying image source model (ISM) method (see Fig. 1). In this method, sound trajectories between a transmitter and a receiver with the known position are represented by mirror sources using the geometric law of reflection. Thus, ISM provides reflectograms, which are correct within the theory of geometrical acoustics [35, 36, 37]. The mathematical approach of ISM method is described in [3] in full detail. Furthermore, these travel-times derived from simulation can be associated to the measured travel-times using the peak detection method which is explained in the following.

2.3. Peak detection

To detect travel-times in the measured reflectogram, the Max criterion or peak detection method is proposed [3], where the maximum argument in the measured impulse response is the estimated travel-time

$$\hat{\tau} = arg\ \max_{t}\{|h(t)|\}, \tag{9}$$

where $\hat{\tau}$ is the detected travel-time and $h(t)$ is the measured impulse response.
Prior to maximization, an analysis time window is centered around each travel-time at the simulated impulse response. This time window is mapped to the measured travel-times to find the maximum peak inside the window [3, 4]. As a result, the time of the maximum peak within each analysis window illustrates the measured travel-time and can be expressed as

$$\tau_i = t_{Start} + \hat{\tau}, \tag{10}$$

where τ_i is the travel-time in a short-term analysis window and t is within a range of $t_{Start} < t < t_{End}$ [3, 4, 38].

2.4. Acoustic travel-time tomography

To solve the inverse problem of reconstructing temperature distribution from measured travel-times, the simultaneous iterative reconstruction technique (SIRT) has been applied. The following two sections expand on the details of tomography calculation.

2.4.1. Simultaneous iterative reconstruction technique (SIRT)

Consider the matrix form of (2) as follows

$$\boldsymbol{A}\boldsymbol{x} = \boldsymbol{b}, \tag{11}$$

where $\boldsymbol{x} \in \mathbb{R}^{V\times 1}$ denotes slowness, $\boldsymbol{A} \in \mathbb{R}^{L\times V}$ includes the distribution of the length of paths contributed within each voxel, and $\boldsymbol{b} \in \mathbb{R}^{L\times 1}$ is the travel-times along each path. The least squares problem is defined as

$$\min_{\boldsymbol{x}} \|\boldsymbol{x} - \boldsymbol{A}^{-1}\boldsymbol{b}\|^2 \tag{12}$$

To solve (12) inversely, the SIRT algorithm employs the least-squares method which minimizes the sum of quadratic differences between the reconstructed slowness i.e., $\boldsymbol{A}^{-1}\boldsymbol{b}$ and slowness i.e., $\boldsymbol{x}$ [3, 4, 21].
To generate the matrix $\boldsymbol{A}$, it requires to calculate the length of all sound paths in each voxel. The sound paths, which have already been calculated by ISM method described in 2.2, can be passed through various defined tomographic voxels. Therefore, each sound path is divided into certain parts, each part is within different voxel. To calculate this division of sound paths, it is essential to detect all intersection points of a sound path with every plane of a voxel. For this purpose, the following algorithm is implemented to construct matrix $\boldsymbol{A}$ as [3, 4, 34]

- Step 1: Construct the coordinates of all voxels by defining voxel planes and voxel origins.
- Step 2: Intersection of 'first order' sound paths with every plane of every voxel.
  - Step 2.1: A vector from source or receiver to the point of the reflection (blue points in Fig. 1).
  - Step 2.2: Intersection between the vectors at step 2.1 with every plane of every voxel.
- Step 3: Intersection of 'second order' sound paths with every plane of every voxel.
  - Step 3.1: Construct vectors from source to first wall reflection (red points in Fig. 1), from first refection point to second reflection (green points in Fig. 1), and from second reflection points to the receiver.
  - Step 3.2: Intersection between the vectors at step 3.1 with every plane of every voxel.
- Step 4: Calculate the length of each vector inside every voxel with regard to the points obtained at step 2 and 3.

- Step 5: Finally, construct the matrix $\boldsymbol{A}$ similar to (13) using step 4.

Therefore, the matrix $\boldsymbol{A}$ can be written in the following form

$$A = \begin{bmatrix} a_{1,1} & a_{1,2} & \cdots & a_{1,V} \\ a_{2,1} & a_{2,2} & \cdots & a_{2,V} \\ \vdots & \vdots & \ddots & \vdots \\ a_{L,1} & a_{L,2} & \cdots & a_{L,V} \end{bmatrix} \tag{13}$$

where $a_{l,v}$ denotes the fraction length of lth sound path at vth voxel.
The SIRT algorithm is applied to reconstruct $\boldsymbol{x}$ in (12) [39, 40, 9]. This method is simultaneous in the sense that all equations are solved at the same time in one iteration [41]. In this study, Landweber's method is applied, which is given by

$$x^{k+1} = x^k + \lambda_k A^T (b - Ax^k),\ k = 0, 1, 2, ..., \tag{14}$$

where x^k represents the current iteration vector stands for slowness values, x^{k+1} is the new iteration vector and λ_k is a relaxation parameter.

2.4.2. Discretization of the tomographic field

Applying the equation (14) in the preceding section requires the subdivision of tomographic area into tomographic voxels whilst the distribution of slowness is assumed to be constant within each voxel. Let V be the number of voxel and L be the total number of travel-times along different propagation paths. In the case of no correlation between the sound paths, the relationship between V and L can be written as

$$\begin{cases} L = V & \text{Just-determined problem;} \\ L < V & \text{Under-determined problem;} \\ L > V & \text{Over-determined problem.} \end{cases} \tag{15}$$

Although the assumption of the current approach is that the total number of travel-times along different propagation paths is greater than the number of voxels, the tomographic problem was treated as under-determined because of the correlations between the given number of sound paths in the tomographic matrix $\boldsymbol{A}$. Therefore, *a priori* information, including the first guess of the searched slowness, was considered to solve the equation (2) [21].

3. Numerical method (optimization)

In this section, the developed numerical method is presented, which helps to optimize transducers location and the sound-ray coverage of the room. This proposed procedure for estimating the optimal coordinates of transducers outlined in 3.1 is valid for any rectangular room. The method calculates the travel-time differences of every sound path up to second order reflections. These differences are adjusted to be above an arbitrary threshold level to separate the reflections at the RIR reflectogram. Moreover, the proposed numerical model ensures the best sound-ray coverage of the room by considering an additional function to avoid having empty tomographic voxels as outlined in 3.2.

3.1. Optimal transmitter and receiver positions

Once a known signal radiates from a sound-source into an enclosed space, the propagating signal is reflected on the boundary surfaces of the enclosure until it reaches the receiver. This relationship is described by the impulse response of the room for each source-receiver combination. The impulse response consists of the travel-times of the direct path and multi-path attenuated reflections. One step to implement the ATOM technique is to detect the measured travel-times of early reflections to associate them to the simulated one. Therefore, these travel-times must be clearly distinguishable on a time-domain reflectogram of the RIR. To avoid overlapping of these early reflections, the position of the transducers should be determined to have the minimum number of simultaneous arrival times. This problem is addressed by presenting a numerical method to find the optimal coordinates of the transducers for the given geometry of the examined rectangular room. Let $\mathcal{V}$ be the dimension of this room defined by

$$\mathcal{V} = \left\{ (x, y, z) \;\middle|\; 0 \le x \le x_0, 0 \le y \le y_0, 0 \le z \le z_0 \right\}. \tag{16}$$

To provide the total number of feasible locations for placement of the transducers, each dimension of the $\mathcal{V}$ is divided into K certain bins. Accordingly, the following equation presents the calculation of the optimal position of transducers. It obtains the solution by minimizing the sum of the number of cases that the time differences between the ith and jth paths are below a desired threshold level Δ for every grid point. These optimal coordinates of transducers allow separation of the travel-times in the RIR reflectogram. Thus, to obtain the optimal coordinates of transmitter and receiver, i.e. $\mathcal{D}$, the following calculation holds,

$$\mathcal{D} \in arg \min_{\{(r_k, s_k)\}} \sum_{i=1}^{L_k} \sum_{j=i+1}^{L_k} \mathbb{I}(\left| t_i(r_k, s_k) - t_j(r_k, s_k) \right| \le \Delta), \tag{17}$$

where $t_i(r_k, s_k)$ and $t_j(r_k, s_k)$ are the travel-times of the early reflections sound paths corresponding to the ith and jth paths, respectively. The direct path is used to find the starting point of the received signal at the RIR reflectorgram and it is excluded from (17). L_k is the total number of sound paths corresponding to the (r_k, s_k)th locations and $\mathbb{I}$ is an indicator function defined as follows

$$\mathbb{I}(x) := \begin{cases} 0 & \text{if } x \text{ is false;} \\ 1 & \text{if } x \text{ is true.} \end{cases} \tag{18}$$

$\mathbb{I}(x)$ maps elements of x to the range of 0 and 1, counting the cases in which $\left| t_i(r_k, s_k) - t_j(r_k, s_k) \right|$ is less than Δ.

Here Δ is a threshold level chosen appropriately according to the desired time differences between the two sound paths, i.e. $\left|t_i(r_k, s_k) - t_j(r_k, s_k)\right|$. If Δ is set to a small value, then smaller number of positions satisfy (17) and for large values it is vice versa. To determine the desired threshold level, it requires to start with a small value (based on the desired time differences between the two sound paths). If no (r_k, s_k) satisfies (17), Δ should be increased to the point where at least one position to be found in the set $\mathcal{D}$.
The (17) aims to separate early reflections as much as possible for having a clear reflectogram. Otherwise, simultaneous sound paths fit into one analysis time-window for peak detection. Hence, it leads to the ambiguity of sound velocity calculation for those paths trapped into one window.

3.2. Maximal sound-ray coverage of the room

Independently from the calculation of the optimal coordinates of transducers, the sound-rays should travel through all parts of the room to spread over the area in a unified manner. The reason is that when some of the voxels remain empty of sound-rays, it degrades the accuracy of the temperature reconstruction. For this purpose, an additional function is employed in the numerical method to set the accumulated travel-times at each voxel above a threshold. Thus, it can be written as

$$\mathcal{C} := \left\{ (r, s) \in \mathcal{V} \;\middle|\; \sum_{i=1}^{L_{r,s}} t_i^{(v)}(r, s) \geq \alpha, \forall v \right\} \tag{19}$$

where $t_i^{(v)}(r, s)$ is the sum of sound travel-times inside the vth voxel corresponding to the source and receiver locations at (r, s), $\mathcal{V}$ is defined in (16), $L_{r,s}$ is the total number of travel-times corresponding to (r, s), and α is a threshold which determines the accumulated travel-times at the vth voxel. Hence, considering (17) and (19), the ultimate solution is the combination of both coverage and distinguishability problems given in the following form

$$(r, s) \in \mathcal{D} \cap \mathcal{C} \tag{20}$$

It is worth noting that there is a trade-off between the results of (17) and (19). In the case of symmetry occurring in the relative locations of sound-source and receiver, maximum sound-ray coverage can be achieved. However, this leads to many overlapping sound-rays. On the contrary, when there is no symmetry, non-overlapping sound-rays appear but the coverage of the room becomes poor. Therefore, it is required to solve both optimization problems by considering the mentioned trade-off.

4. Practical implementation

The experimental set-up was performed to test the fidelity of the numerical method presented. For this purpose, the climate chamber lab of the Bauhaus-University Weimar was chosen as a test space. Fig. 2 illustrates the measurement set-up containing the location of the transmitter, receiver, and NTC thermistors. The chamber measures 3 m (width) by 3 m (length) by 2.44 m (height) and is able to create temperatures between $+10°C$ and $+40°C$. This controllable condition ensures the main advantages, such as the ability to set a wide range of temperature variations while it generates minimum convection within the measurement area. The chamber was tempered only by its 6 surfaces, resulting in a homogeneous air temperature. As all 6 surfaces had a similar temperature and ventilation was turned off, no forced convection occurred inside the chamber. More details about the characteristics of the climate chamber are provided in [42].

Figure 2: Experimental set-up in the climate chamber lab of the Bauhaus-University Weimar. 1) four of the eight mounted NTC thermistors which are superimposed, 2) receiver, and 3) transmitter

In this experiment, first, one source and one receiver were located at non-optimal positions, which were selected randomly. Hence, the theoretical sound-ray paths up to second order reflections are simulated using the same convention of the ISM provided in [4, 3]. Furthermore, the optimal positions of transducers for the given geometry of the climate chamber were calculated. For this purpose, each dimension of the room is divided into 20 segments; the total number of feasible coordinates is $K = 20^3$ [28]. The threshold level

Table 1
Transducers coordinates

Alternatives	Coordinates	
Non-opt-position	source	receiver
(randomly selected)	$x = 1.90$ m	$x = 1.20$ m
	$y = 2.50$ m	$y = 0.40$ m
(session 1 and 3)	$z = 1.50$ m	$z = 0.90$ m
Opt-position	source	receiver
(calculated)	$x = 0.69$ m	$x = 0.25$ m
	$y = 1.72$ m	$y = 0.69$ m
(session 2 and 4)	$z = 1.18$ m	$z = 0.60$ m

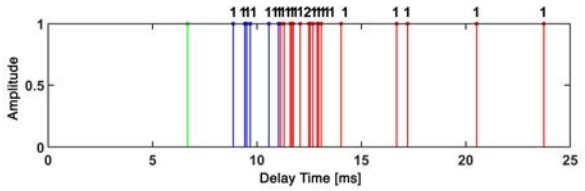

(a) Non-optimal position

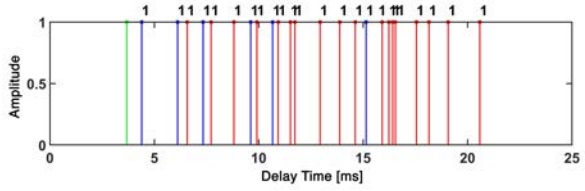

(b) Optimal position

Figure 3: Comparing the reflectograms of (a) non-optimal and (b) optimal case. The number above the lines shows the number of sound paths arriving at that time within a threshold level of 0.1 ms. The order – green line: direct sound; blue lines: first order reflections; red lines: second order reflections – means how many times a sound signal is reflected at the room boundaries when traveling along the sound path from transmitter to receiver.

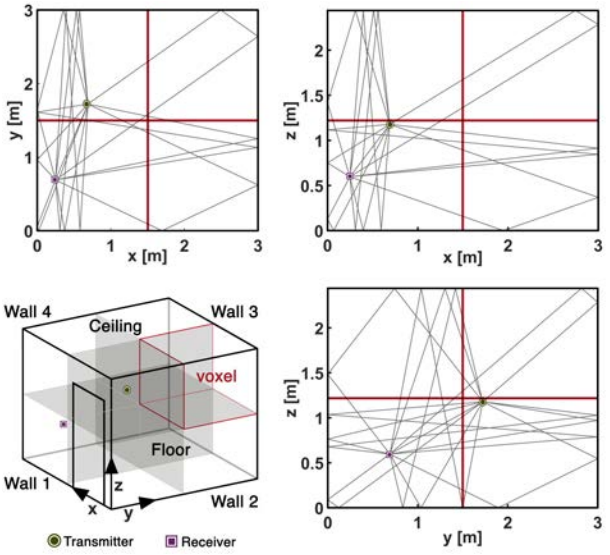

Figure 4: Subdivision of tomographic area. Each dimension of the room was divided in two parts evenly.

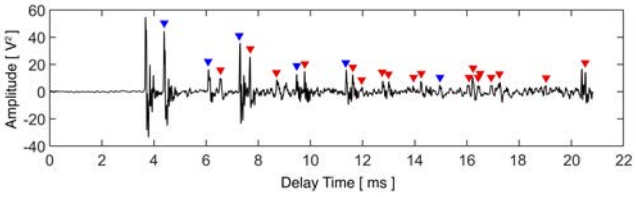

Figure 5: Calculated impulse response of the measured signal. The arrow signs above the reflections illustrate the selected travel-times, blue arrow signs are first order and red arrow signs are second order reflections.

was set to $\Delta = 0.5$ ms, determined based on the desired time differences of the sound paths. To illustrate the impact of the optimal coordinates of the transducers on the RIR, the simulated reflectogram of non-optimal positions is compared to the simulated reflectogram of optimal positions; their coordinates are outlined in Table 1.

Fig. 3a depicts the results of the image source model for the non-optimal positions. The horizontal axis shows travel-times of the sound paths up to second order reflections. Accordingly, each line corresponds to the arrival time of a sound signal at the receiver. The vertical axis presents the amplitude of the sound paths. As in this simulation only the time of arrival of the sound signals is of interest, no energy is converted in the calculation model and all incoming sound paths still have one hundred percentage of the sound energy. The number above the vertical lines shows the number of sound paths arriving at that certain time. It is evident that for the non-optimal position, the travel-times are very close to each other. As the measurement environment includes noises and scattering, this distribution of travel-times leads to several overlapping sound paths, which arrived simultaneously in the measured RIR. However, as it is shown in Fig. 3b, all the sound paths up to second order reflections for the optimal case have different travel-times and each line represents only one sound-ray path. This comparison of simulated reflectograms demonstrates that the optimal position of the sound-source and receiver leads to an optimized distribution of travel-times in the reflectogram.

For the tomographic reconstruction, the volume of the chamber has been divided into $2^3 = 8$ voxels. Therefore, the volume of each voxel is $(x \cdot y \cdot z) = (1.5\text{ m} \cdot 1.5\text{ m} \cdot 1.22\text{ m})$. This subdivision of the tomographic area is outlined in Fig. 4. To compare the tomographically reconstructed temperatures with *in-situ* measurements, eight temperature sensors (NTC- negative temperature coefficient thermistors) with an accuracy of ± 0.1K were applied at the center of the eight tomographic voxels. The measurement interval of the NTC thermistors was set to 1 second. The calculation time of ATOM measurement was selected based on the length of the excitation signal, the power of the computer for execution of cross-correlation, peak detection and tomographic reconstruction. Furthermore, to minimize noise and scattering errors, the RIR was averaged over fifty reflectograms. Thus, the ATOM temperatures are calculated for every 2 minutes, considering the both calculation time and the time of the RIR averaging. Accordingly, the data of the NTC thermistors, which are synchronized with the ATOM measurement, were recorded and averaged. Finally, the average temperatures at each voxel were compared with the averaged-point temperatures of NTC thermistors.

Fig. 5 illustrates an example of the calculated impulse response of the measured signal conducted for the optimal coordinates of the transducers in the climate chamber. The number of sound paths for the given coordinates of transducers was 24, six first-order reflections (blue arrow signs) and eighteen second-order reflections (red arrow signs). To detect the travel-times, the simulated travel-times derived

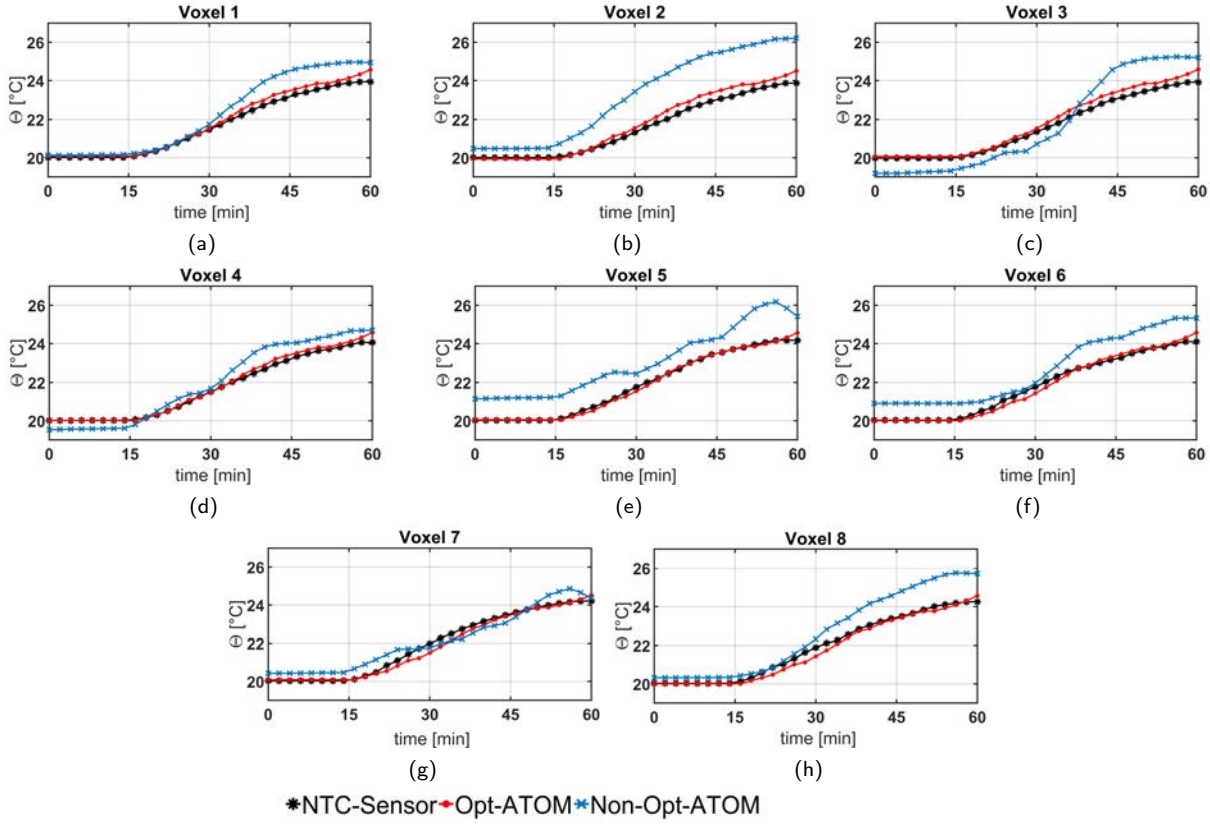

Figure 6: Measurement results during sessions 1 and 2 (Table 2), comparison of the temperatures of the NTC thermistors with ATOM temperatures for the both optimal and non-optimal cases within eight voxels separately.

from ISM method are used to locate the centre of an analysis time-window at this measured RIR reflectogram. Consequently, the maximum peak inside the analysis time-window was considered as the selected travel-time.

The experiment was conducted under a gradual air temperature drift from $\theta = 20°C$ to $\theta = 24°C$ during one hour and vice versa. These temperature drifts have been chosen to test the performance of the developed ATOM method even under transient conditions. Moreover, as the corresponding temperature drifts are within the range of acceptable thermal conditions of a normal office, a prospective scenario is to use the ATOM temperatures as the input data for the thermal comfort analysis of an office environment.

The total of four experimental sessions were conducted as listed in Table 2. Session 1 and 2 were considered as the increasing cases, meaning that, during these sessions, the temperature increased from $\theta = 20°C$ to $\theta = 24°C$ gradually. In reverse, sessions 3 and 4 were regarded as decreasing cases, illustrating the process of dropping the temperature from $\theta = 24°C$ to $\theta = 20°C$.

Table 2
Sessions of the experiment

Sessions	Location	Temp-Drift[$°C$]	Duration[min]
1	Non-opt	20 to 24	60
2	Opt	20 to 24	60
3	Non-opt	24 to 20	60
4	Opt	24 to 20	60

The sound source used in the measurement was a special self-constructed speaker (with a 2-inch broadband driver FRS 5 XTS by VISATON). It was developed to have a nearly omni-directional point source; its specification are detailed in [3]. The receiver was a standard 1/4-inch condenser microphone of type 'AVM8 MI-17'. For data acquisition, the measurement card 'Data Translation DT9847-2-2' was used, which is a dual channel dynamic signal analyser. The digitization rate of 216 kHz leads to a good time-resolution for the processing of signals. This rate of sampling frequency was required for the small dimensions of the climate chamber lab resulted in short sound travel-times. In contrast to big room spaces, the small dimension of the climate chamber causes the reflections up to the second order arrive at the receiver in a short period of time, around 25ms. Thus, the reflectogram of the impulse response requires to have a proper resolution of those condensed travel-times to be able to distinguish them. The sampling frequency of 216 kHz provides enough resolution, circa 4.6 μs resulted in reducing the error of travel-time estimate. For this sampling frequency, an excitation time of 1.21 s for the MLS-signal was used. The software package used to analyse the data is MATLAB R2017b.

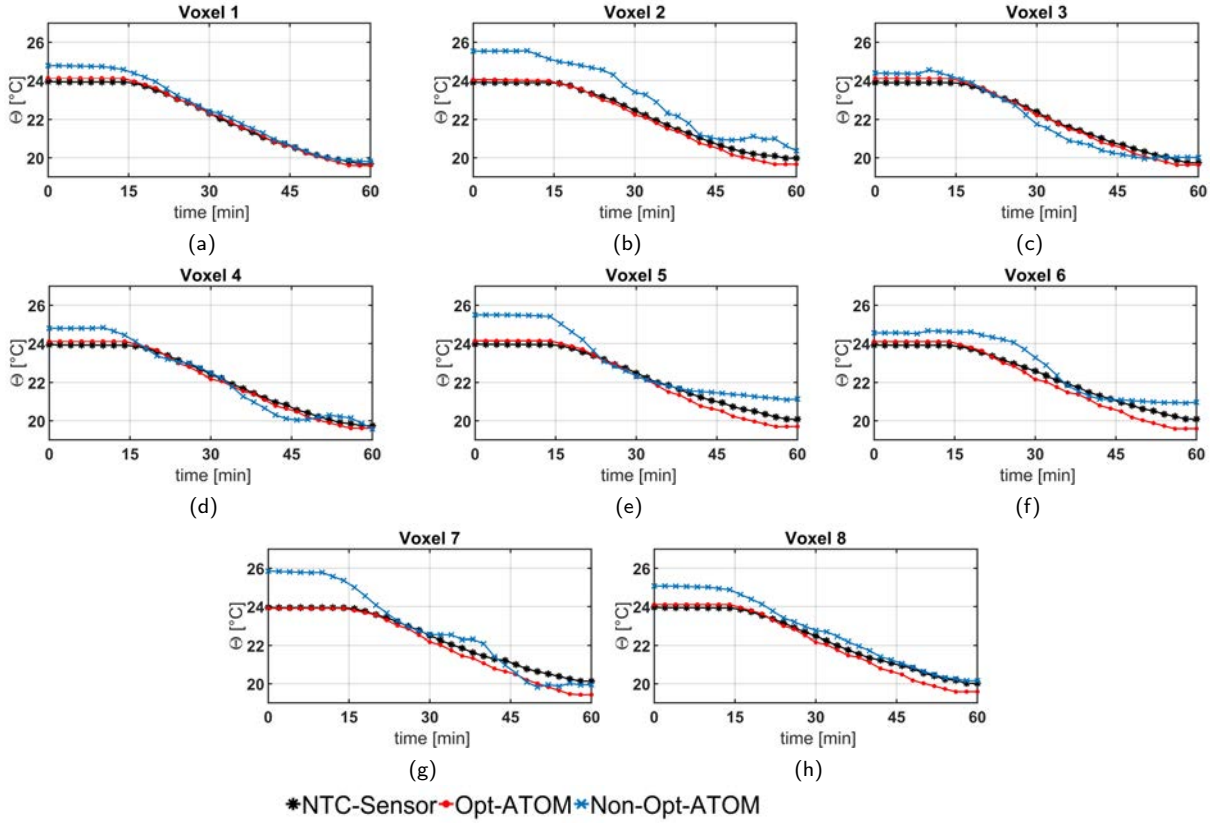

Figure 7: Measurement results during sessions 3 and 4 (Table 2), comparison of the temperatures of the NTC thermistors with ATOM temperatures for the both optimal and non-optimal cases within eight voxels separately.

5. Measurement results and data analysis

The point temperature of each voxel was measured by NTC thermistors while the average temperatures of individual voxels were obtained by the ATOM technique simultaneously. Fig. 6 illustrates the comparison of temperatures between the NTC thermistors and ATOM for both optimal and non-optimal positions during session 1 and 2. It is evident that the ATOM temperatures of the non-optimal positions deviated from the NTC thermistors, although the amount of deviations varies at every voxel. For example, in Fig. 6d and 6g (representing voxels 4 and 7, respectively), the deviations of the non-optimal profile from NTC thermistors are relatively constant through the entire measurement. On the contrary, in Fig. 6a and 6h (representing voxels 1 and 8, respectively), the non-optimal curves show larger deviations from NTC thermistors, which occurred after the first 30 minutes of the experiment. One would associate such deviations from NTC thermistors with multiple simultaneous arrival times of individual paths at the non-optimal case.
The overlapping sound-paths reduce the accuracy of the peak detection method in noisy and scattering environments. Therefore, inaccurate peak detection introduces errors to vector $\boldsymbol{b}$ at (12). This causes the error to be spread over all voxels, as the set of equations at (11) should be solved simultaneously. Fig. 7 compares the temperature variations of the ATOM and NTC thermistors during session 3 and 4. It is observed that the greatest deviation of temperature occurred for the non-optimal case similar to the session 2. Conversely, the ATOM technique responds to the temperature variations to some extent in line with the NTC thermistors for the optimal case. For instance, in voxel 4 outlined in Fig. 7d, during the first 10 minutes of the experiment, the difference of temperature between the optimal case and NTC thermistors is about $0.2°C$ while this difference is about $0.88°C$ for the non-optimal case. Thus, at this certain time, optimizing the location of transducers enhances the accuracy of temperature distributions about $0.68°C$ in comparison to non-optimal position.
Fig. 8 outlines the three-dimensional representation of temperature distributions measured by ATOM technique during session 1 and 2 for the non-optimal and optimal coordinates. The color-bar represents temperatures increasing from $20°C$ to $24°C$ within each voxel over time. Fig. 8a, 8b and 8c show a non-uniform variation of temperatures for the non-optimal case during session 1, demonstrating the amount of deviations occurred in each voxel. Conversely, Fig. 8d, 8e and 8f illustrates the temperature distribution of the optimal case indicating that the temperature varies uniformly across the room as the six surfaces of the climate chamber were tempered simultaneously. To determine the differences between the results of the tomography calculation and NTC thermistors, the root mean square error (RMSE) for each voxel can

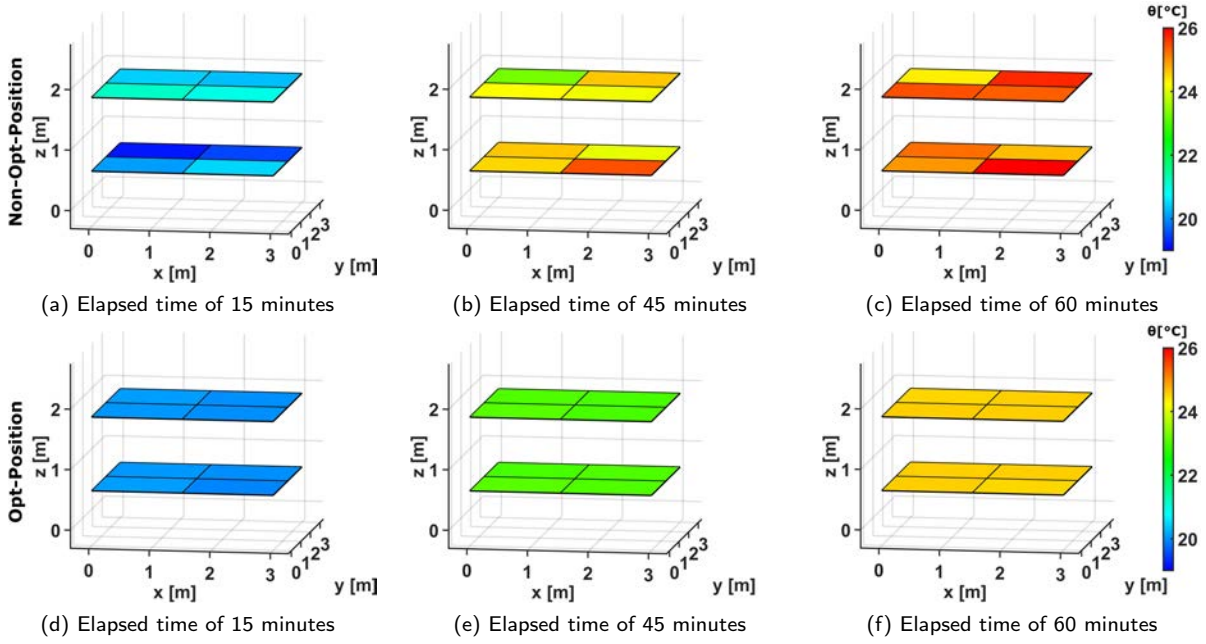

(a) Elapsed time of 15 minutes (b) Elapsed time of 45 minutes (c) Elapsed time of 60 minutes

(d) Elapsed time of 15 minutes (e) Elapsed time of 45 minutes (f) Elapsed time of 60 minutes

Figure 8: Three-dimensional representation of ATOM temperature distribution for the non-optimal (session 1) and optimal (session 2) positions. The color-bar of the optimal position illustrates the uniform variations of the temperatures inside the chamber in contrast to the non-optimal one.

be calculated as

$$RMSE = \sqrt{\frac{\sum_{n=1}^{N}(T_{ATOM}^{n} - T_{NTC}^{n})^2}{N}} \tag{21}$$

where T_{ATOM}^{n} is the ATOM temperature, T_{NTC}^{n} is the temperature of NTC thermistors and N is the total number of measurements over time [21]. Fig. 9 illustrates the RMSE calculation for the entire sessions as a statistical evaluation over all eight voxels. The small RMSE, which is less than $0.44°C$ during sessions 2 and 4, demonstrates the positive impact of the optimal position on the tomography results. Table 3, derived from Fig. 9, shows the maximum (max), average (ave), median (med) and minimum (min) RMSE of all sessions. It is observed that during session 1 and 2, the results of the optimal case are approximately $1.48°C$ (max) and $0.71°C$ (ave) more accurate in comparison to non-optimal case in maximum and average RMSE among all voxels, respectively. Furthermore, during session 3 and 4, the results derived from the optimal case are approximately $0.7°C$ (max) and $0.36°C$ (ave) more accurate than non-optimal case in maximum and average RMSE among all voxels, respectively.

Table 3
Maximum, average, median and minimum RMSE averaged over all eight voxels

Sessions	Max [$\circ C$]	Ave [$\circ C$]	Med [$\circ C$]	Min [$\circ C$]
1 - Non-opt	1.83	0.99	0.84	0.57
2 - Opt	0.35	0.28	0.28	0.22
3 - Non-opt	1.14	0.69	0.59	0.38
4 - Opt	0.44	0.33	0.32	0.22

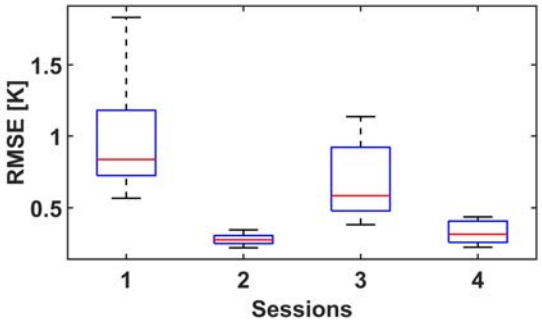

Figure 9: The root mean square error (RMSE) between the ATOM temperatures and NTC thermistors for each session, averaged over all voxels; black lines: maximum and minimum RMSE, red line: median RMSE, blue lines: 80%/20% quantile RMSE

6. Conclusions

In this study, to measure the spatially distributed, indoor air temperature using the ATOM technique, a numerical method was proposed to determine an optimal position of transducers, which simultaneously achieves good sound-rays coverage of the room. The former makes the arrival time of the sound-rays distinguishable and the latter assists the existence of sound-rays over all voxels. Therefore, the ATOM temperatures can be measured satisfactory given two conditions. Firstly, the transducers are placed at the proper coordinates, which are derived from numerical calculation for a given geometry. Secondly, a trade-off between the results of optimal position of transducers and the maximal

sound-ray coverage of the room at the optimal position is considered. Future research could examine the application of ATOM technique in an inhomogeneous room climate.

Acknowledgments

This work was supported by the Thüringer Graduiertenförderung. Additionally, we highly appreciate the scientific collaboration with Dr. Armin Raabe from the Institute of Meteorology, University of Leipzig and his team including M.Sc. Marcus Bleisteiner and Dr. Manuela Starke.

References

[1] Y. Li, S. Liu, S. Inaki, Dynamic reconstruction algorithm of three-dimensional temperature field measurement by acoustic tomography, Sensors 17 (9) (2017) 2084.

[2] I. Jovanovic, L. Sbaiz, M. Vetterli, Acoustic tomography method for measuring temperature and wind velocity, in: 2006 IEEE International Conference on Acoustics Speech and Signal Processing Proceedings, Vol. 4, IEEE, 2006, pp. IV–IV.

[3] M. Bleisteiner, M. Barth, A. Raabe, Tomographic reconstruction of indoor spatial temperature distributions using room impulse responses, Measurement Science and Technology 27 (3) (2016) 035306.

[4] M. Barth, A. Raabe, Acoustic tomographic imaging of temperature and flow fields in air, Measurement Science and Technology 22 (3) (2011) 035102.

[5] M. Barth, Akustische tomographie zur zeitgleichen Erfassung von temperatur-und Strömungsfeldern, Institut für Meteorologie der Universität Leipzig, 2009.

[6] X. Mao, Acoustic techniques for temperature and flow velocity measurements, Citeseer, 2005.

[7] M. Barth, A. Raabe, K. Arnold, C. Resagk, R. Du Puits, Flow field detection using acoustic travel time tomography, Meteorologische Zeitschrift 16 (4) (2007) 443–450.

[8] S. Liu, S. Liu, G. Tong, Reconstruction method for inversion problems in an acoustic tomography based temperature distribution measurement, Measurement Science and Technology 28 (11) (2017) 115005.

[9] H. Zhu, H. Yan, L. LIu, An optimized iterative reconstruction algorithm for three-dimensional temperature field, in: Proceedings of the International Conference on Graphics and Signal Processing, ACM, 2017, pp. 91–95.

[10] H. Yan, S. H. Wang, Y. G. Zhou, L. J. Liu, A 3d acoustic temperature field reconstruction algorithm using adaptive regularization parameter, in: 2013 IEEE International Conference on Imaging Systems and Techniques (IST), IEEE, 2013, pp. 150–154.

[11] Y. Liu, H. Schlaberg, S. Liu, S. Ren, Acoustic tomography of temperature and wind flow fields in a wind power plant, 2nd IET Renewable Power Generation Conference (RPG 2013) (2013).

[12] P. Holstein, A. Raabe, R. Müller, M. Barth, D. Mackenzie, E. Starke, Acoustic tomography on the basis of travel-time measurement, Measurement Science and Technology 15 (7) (2004) 1420.

[13] D. A. Bohn, Environmental effects on the speed of sound, J. Audio Eng. Soc 36 (4) (1988) 223–231.
URL http://www.aes.org/e-lib/browse.cfm?elib=5156

[14] H. Yan, Z. Ma, Y. G. Zhou, Acoustic tomography system for online monitoring of temperature fields, IET Science, Measurement & Technology 11 (5) (2017) 623–630.

[15] I. Jovanović, L. Sbaiz, M. Vetterli, Acoustic tomography for scalar and vector fields: theory and application to temperature and wind estimation, Journal of Atmospheric and Oceanic Technology 26 (8) (2009) 1475–1492.

[16] Y. Bao, J. Jia, N. Polydorides, Real-time temperature field measurement based on acoustic tomography, Measurement Science and Technology 28 (7) (2017) 074002.

[17] Y. Bao, J. Jia, Real-time wind velocity monitoring based on acoustic tomography, in: Geological Disaster Monitoring Based on Sensor Networks, Springer, 2019, pp. 135–149.

[18] T. Sato, H. Aoki, O. Ikeda, Introduction of mass conservation law to improve the tomographic estimation of flow-velocity distribution from differential time-of-flight data, The Journal of the Acoustical Society of America 77 (6) (1985) 2104–2106.

[19] D. Keith Wilson, D. W. Thomson, Acoustic tomographic monitoring of the atmospheric surface layer, Journal of Atmospheric and Oceanic Technology 11 (3) (1994) 751–769.

[20] G. Tetzlaff, K. Arnold, A. Raabe, A. Ziemann, Observations of area averaged near-surface wind-and temperature-fields in real terrain using acoustic travel time tomography, Meteorologische Zeitschrift 11 (4) (2002) 273–283.

[21] G. Fischer, M. Barth, A. Ziemann, Acoustic tomography of the atmosphere: comparison of different reconstruction algorithms, Acta Acustica United with Acustica 98 (4) (2012) 534–545.

[22] K. Arnold, A. Ziemann, A. Raabe, Acoustic tomography in comparision to in-situ temperature and wind measurements, Wissenschaftliche Mitteilungen aus dem Institut für Meteorologie der Universität Leipzig (2001).

[23] S. N. Vecherin, V. E. Ostashev, D. K. Wilson, Assessment of systematic measurement errors for acoustic travel-time tomography of the atmosphere, The Journal of the Acoustical Society of America 134 (3) (2013) 1802–1813.

[24] H. Yan, Z. Peng, K. Cui, L. Zhang, Acoustic travel-time measurement in acoustic temperature field monitoring, in: Intelligent Control and Automation, 2008. WCICA 2008. 7th World Congress on, IEEE, 2008, pp. 4947–4951.

[25] V. E. Ostashev, D. K. Wilson, Acoustics in moving inhomogeneous media, CRC Press, 2015.

[26] O. Cramer, The variation of the specific heat ratio and the speed of sound in air with temperature, pressure, humidity, and co2 concentration, The Journal of the Acoustical Society of America 93 (5) (1993) 2510–2516.

[27] Y. Bao, J. Jia, Nonlinear temperature field reconstruction using acoustic tomography, in: 2017 IEEE International Conference on Imaging Systems and Techniques (IST), IEEE, 2017, pp. 1–6.

[28] N. S. Dokhanchi, J. Arnold, A. Vogel, C. Voelker, Acoustic travel-time tomography: Optimal positioning of transceiver and maximal sound-ray coverage of the room, in: Fortschritte der Akustik - DAGA 2019, 2019, p. 23–26.

[29] M. Vorländer, M. Kob, Practical aspects of mls measurements in building acoustics, Applied Acoustics 52 (3-4) (1997) 239–258.

[30] F. Policardi, Mls and sine-sweep measurements, Università di Bologna, Italia ELEKTROTEHNIŠKI VESTNIK 78 (3) (2011) 91–95.

[31] P. Guidorzi, L. Barbaresi, D. D'Orazio, M. Garai, Impulse responses measured with mls or swept-sine signals applied to architectural acoustics: an in-depth analysis of the two methods and some case studies of measurements inside theaters, Energy Procedia 78 (2015) 1611–1616.

[32] X. Wang, Model based signal enhancement for impulse response measurement, Vol. 18, Logos Verlag Berlin GmbH, 2014.

[33] M. Holters, T. Corbach, U. Zölzer, Impulse response measurement techniques and their applicability in the real world, in: Proceedings of the 12th International Conference on Digital Audio Effects (DAFx-09), 2009, pp. 1–5.

[34] M. Bleisteiner, Ableitung von Raumtemperaturverteilungen aus Schallreflexionsmessungen, Technische Universität Berlin, 2014.

[35] P. Mehta, V. Bhadradiya, Measurement of room impulse response using image source method, in: 2015 International Conference on Electrical, Electronics and Mechatronics, Atlantis Press, 2015, pp. 101–103.

[36] E. A. Habets, Room impulse response generator, Technische Universiteit Eindhoven, Tech. Rep 2 (2.4) (2006) 1.

[37] J. Borish, Extension of the image model to arbitrary polyhedra, The Journal of the Acoustical Society of America 75 (6) (1984) 1827–

1836.
[38] S. Tervo, J. Pätynen, T. Lokki, Acoustic reflection localization from room impulse responses, ACTA Acustica united with Acustica 98 (3) (2012) 418–440.
[39] A. H. Andersen, A. C. Kak, Simultaneous algebraic reconstruction technique (sart): a superior implementation of the art algorithm, Ultrasonic imaging 6 (1) (1984) 81–94.
[40] M. Jiang, G. Wang, Convergence of the simultaneous algebraic reconstruction technique (sart), IEEE Transactions on Image Processing 12 (8) (2003) 957–961.
[41] P. C. Hansen, M. Saxild-Hansen, Air tools—a matlab package of algebraic iterative reconstruction methods, Journal of Computational and Applied Mathematics 236 (8) (2012) 2167–2178.
[42] C. Voelker, S. Maempel, O. Kornadt, Measuring the human body's microclimate using a thermal manikin, Indoor Air 24 (6) (2014) 567–579.